Chinese Chemical Letters 34 (2023) 107669

Contents lists available at ScienceDirect

Chinese Chemical Letters

journal homepage: www.elsevier.com/locate/cclet

Amorphous nickel borate nanosheets as cathode material with high capacity and better cycling performance for zinc ion battery

Na Li[a], Xixi Zhang[a], Shunshun Zhao[b], Chuanlin Li[a], Xiaojuan Li[a], Tongkai Wang[a], Yupeng Xing[a], Gangmeng Qu[a], Xijin Xu[a,*]

[a] School of Physics and Technology, University of Jinan, Ji'nan 250022, China
[b] School of Electronic and Information Engineering (Department of Physics), Qilu University of Technology (Shandong Academy of Sciences), Ji'nan 250353, China

ARTICLE INFO

Article history:
Received 20 May 2022
Revised 16 June 2022
Accepted 6 July 2022
Available online 12 July 2022

Keywords:
Amorphous
Nickel borate
Nanosheets structure
Alkaline
Aqueous zinc ion battery

ABSTRACT

Zinc-ion batteries are under current research focus because of their uniqueness in low cost and high safety. However, the pursuing of high-performance cathode materials of aqueous Zinc ion batteries (AZBs) with low cost, high energy density and long cycle life has become the key problem to be solved. Herein we synthesized a series of amorphous nickel borate (AM-NiBO) nanosheets by varying corrosion time with *in-situ* electrochemical corrosion method. The AM-NiBO-T13 as electrode material possesses a high areal capacity of 0.65 mAh/cm^2 with the capacity retention of 95.1% after 2000 cycles. In addition, the assembled AM-NiBO-T13//Zn provides high energy density (0.77 mWh/cm^2 at 1.76 mW/cm^2). The high areal capacity and better cycling performance can be owing to the amorphous nanosheets structure and the stable coordination characteristics of boron and oxygen in borate materials. It shows that amorphous nickel borate nanosheets have great prospects in the field of energy storage.

With the emergence of new technologies such as electric vehicles, wearable electronic devices, and renewable energy storage systems, there is an ever-increasing demand for high performance-batteries [1–3]. Lithium ion battery has developed into a large-scale secondary battery because of its high energy density and long cycle life. However, considering the increasing depletion of lithium reserves and the potential safety hazards and environmental pollution, it is urgent to develop a new safe, environmental friendly and low-cost secondary battery system [4–8]. Rechargeable polyvalent ion batteries utilizing magnesium, zinc, calcium or aluminum ions have attracted extensive attention as candidates, mainly due to their advantages of abundant composition, safety and potential of higher energy density [6,9]. In particular, aqueous zinc ion batteries (AZBs) have become one of the most concerned battery technologies due to the abundant zinc, low redox potential (−1.249 V in alkaline solutions, *vs.* SHE), high volume specific capacity (5851 mAh/cm^3) and theoretical specific capacity (820 mAh/g), high electrochemical stability and compatibility in aqueous electrolyte [10–12]. Generally, alkaline AZIB directly uses metal zinc as the anode electrode, alkaline zinc salt solution as the electrolyte, but looking for cathode materials of aqueous ZIBs with low cost, high energy density and long cycle life has become the key issues [13]. A variety of cathode materials have been explored for AZIBs, such as nickel hydroxide [14–18], nickel sulfide [19–22] and nickel borate [23] and other nickel/cobalt based materials [24–29]. Among these cathode materials, nickel-based materials are considered to be one of the most suitable cathodes for AZIBs owing to their natural abundance, low cost and multivalent state of nickel. For example, the β-NQNC//Zn cell prepared by Chen *et al.* has an ideal area specific capacity (0.34 mAh/cm^2) [30]. But low conductivity and poor cycle stability of $Ni(OH)_2$ limit achievement of high specific capacity at a high charge-discharge rate [31–33].

To overcome the limitation of the cathode material based on a single nickel base, boron is introduced into the structure. The lower atomic weight of boron leads to a higher specific capacity of borate [34,35]. For instance, Xu *et al.* synthesized $Ni_3(BO_3)_2$ by a simple solid-state reaction method and used it as the cathode material of sodium ion battery. The $Ni_3(BO_3)_2$ exhibits a high capacity of 304.4 mAh/g even at 2 A/g [36]. In addition, the introduction of B is conducive to the high reversibility of oxygen redox reaction and maintains good structural stability, so as to improve the good cycle stability [37,38]. Guo *et al.* reported a doping strategy by incorporating light-weight boron into the cathode active ma-

* Corresponding author.
E-mail address: sps_xuxj@ujn.edu.cn (X. Xu).

https://doi.org/10.1016/j.cclet.2022.07.012
1001-8417/

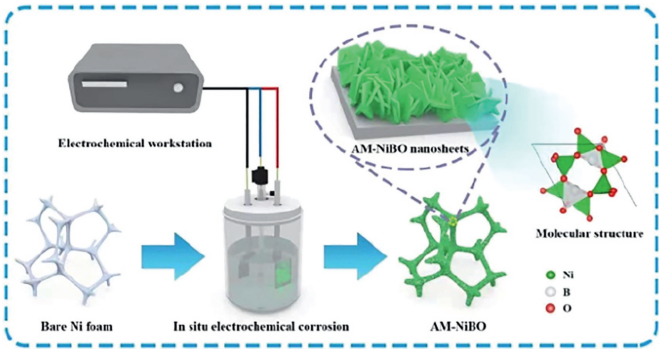

Fig. 1. Schematic diagram of the synthesis process for AM-NiBO.

terial lattice to decrease the irreversible oxygen oxidation at high voltages (*i.e.*, >4.0 V *vs.* Na^+/Na), and the B-substituted NLNFMB thus delivers much better capacity retention (76.3%) than that of B-free NLNFM (45.1%) after 80 cycles at 25 mA/g [39].

Amorphous materials are also capable of achieving better capacitive performance due to their disordered long-range order, metastable structure and inherent abundant defects [40–42]. Tong *et al.* successfully prepared amorphous Co-B-W/O with uniform distribution and assembled alkaline secondary batteries. Meanwhile, the capacity of amorphous Co-B-W/O is 347 mAh/g at 100 mA/g, which is better than the conventional Co-B capacity of 254 mAh/g. In addition, it is worth mentioning that the alkaline secondary battery assembled by the Co-B-W/O has a good cycling performance, because the crystallization of the Co-B-W/O is effectively inhibited during the cycling process [43]. Amorphous nickel borate material has high specific capacity and excellent cycling performance, which is expected to be used as a cathode material to assemble zinc ion batteries.

Amorphous nickel borate (AM-NiBO) was synthesized by *in situ* electrochemical corrosion, which has enhanced physical and chemical properties induced by the nanosheets architecture, large conductivity and high inherent activity. The AM-NiBO-T13 possesses the capacity of 0.65 mAh/cm^2 with the capacity retention rate of 95.1% after 2000 cycles. The assembled AZBs with nickel borate as cathode electrode and zinc as anode materials has the capacity of 0.4 mAh/cm^2, Furthermore, its energy density can reach 0.77 mWh/cm^2 at 1.76 mW/cm^2.

As shown in Fig. 1, AM-NiBO is synthesized by one-step *in-situ* potentiostatically electrochemical corrosion on nickel foam in 0.1 mol/L $K_2B_4O_7$ solution. The thin nanosheets are arranged in disorder with the thickness of a single nanosheet of about 26 nm. The nanosheet structure increases the specific surface area, which is conducive to increasing the electrochemical active sites, shortening the diffusion distance of electrolyte ions, and accelerating the electrical response, thereby improving the utilization efficiency of electrode materials in electrochemical reactions [44]. As shown in Fig. 1, metal atoms are directly combined with oxygen atoms to form boron-oxygen tetrahedrons, as the bond energy is large and relatively stable, so it nickel borate has good structural stability.

SEM images in Figs. 2a and b show the uniform growth of AM-NiBO on the surfaces of nickel foam. In Fig. 2b, these nanosheets are disorderly arranged with small sizes and thickness (about 26 nm). The nanosheets inherit the monodisperse form of AM-NiBO, ensuring the mechanical robustness of the electrode and the full penetration of electrolyte. Two dimensional nanosheets have large specific surface area and excellent mechanical/chemical stability. Low-magnified SEM images are also placed in Fig. S1 (Supporting information). It can be seen from Fig. S1a that nickel foam has good pore structure, large specific surface area. Besides, the foam nickel is a suitable substrate with good conductivity and low

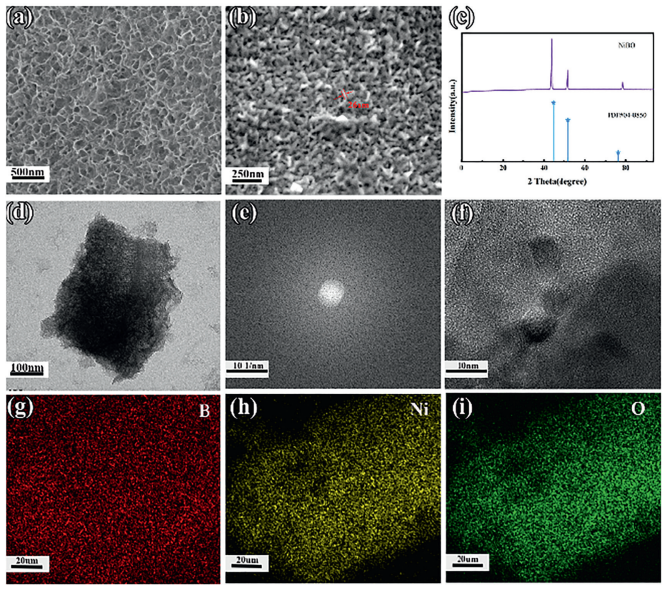

Fig. 2. Characterization of AM-NiBO-T13: (a, b) SEM images; (c) XRD pattern; (d) TEM image; (e) SAED; (f) lattice diffraction diagram and (g-i) elemental mappings.

price. As shown in Figs. S1b and c, disordered nanosheets cover the surface of nickel foam, increasing its surface area and providing more reaction sites for transformation reaction. XRD pattern in Fig. 2c shows that all the observed diffraction peaks are indexed to Ni peaks (PDF#04-0850) [45,46], and no AM-NiBO peak can be observed, partially indicating the amorphous characteristic of AM-NiBO. The XRD of Cr-NiBO can be seen from Fig. S2 (Supporting information) that the material is crystalline, and its capacity is lower than that of AM-NiBO-T13.

TEM image in Fig. 2d presents tiny nanosheet architecture of AM-NiBO. SAED and HRTEM measurements in Figs. 2e and f show that a broad and diffused halo ring and no diffraction points can be observed in SAED image and no long-range ordered lattice fringes are observed in HRTEM image, proving that the atomic arrangement in AM-NiBO is not periodic, so it is concluded that AM-NiBO is in an amorphous state. As known, amorphous materials are characterized by a large number of interior defects and a large number of undercoordinated atoms or reaction sites on the surfaces [47]. Then, the defective and amorphous AM-NiBO provides a relatively fast diffusion rate for protons, and the amorphous structure contributes to the structural stability of electrode materials [48,49]. The element mappings in Figs. 2g-i show that the elements of Ni, B and O are evenly distributed.

The chemical composition and valence states of AM-NiBO are further studied by XPS. The survey spectrum in Fig. 3a depicts the coexistence of Ni, B and O elements. As shown in Fig. 3b, Ni 2p spectrum is well fitted with two spin-orbit doublets, which are characteristic of Ni^{3+} and Ni^{2+}, and two shake-up satellites. Peaks at 856.4 and 874.2 eV are associated with Ni $2p_{3/2}$ and Ni $2p_{1/2}$ of Ni^{2+}, respectively, and two additional shoulder peaks at 855.1 and 872.7 eV are of Ni^{3+} [50]. The two satellite peaks of Ni correspond to 861.2 and 879.5 eV. The peak at 191.5 eV (Fig. 3c) corresponds to B 1s [37]. In Fig. 3d, the peaks at 530.5 and 532 eV corresponds to the B-O and Ni-O bonds, respectively [38].

The comparison of CV curves under different electrochemical corrosion time in Fig. 4a shows that the area surrounded by the CV curve of NiBO-T13 is the largest, indicating the greatest capacity. GCD curves for NiBO-T10-16 in Fig. 4b exhibit the maximum capacity of 0.65 mAh/cm^2 for NiBO-T13. The data of other comparative experiments are shown in Fig. S3 (Supporting infor-

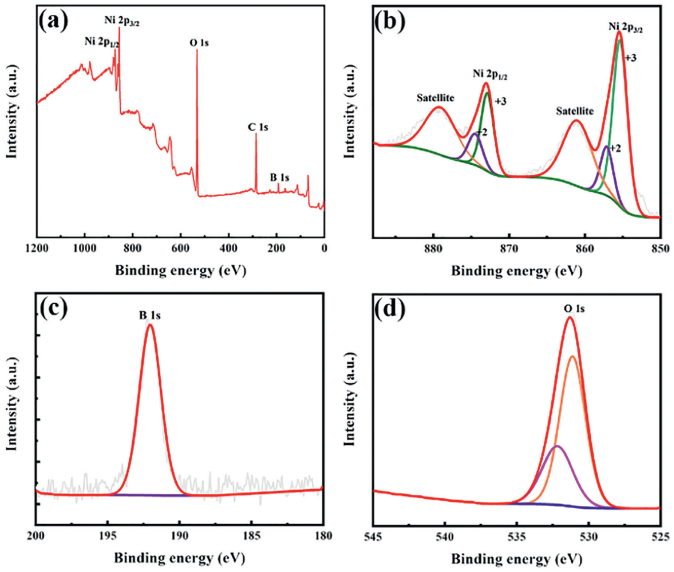

Fig. 3. (a) XPS survey spectrum of AM-NiBO-13. The high resolution spectra of (b) Ni, (c) B and (d) O.

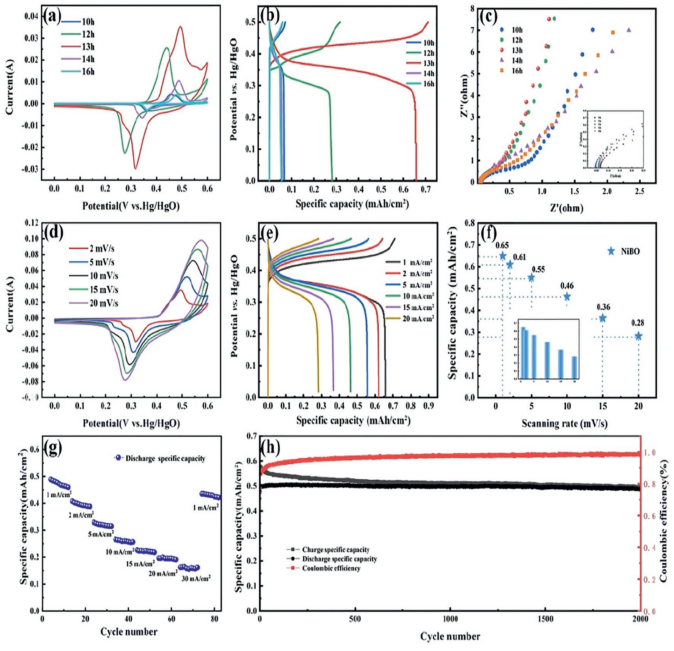

Fig. 4. (a) CV curves of NiBO-T10-16 at 1 mV/s. (b) GCD curves of NiBO-T10-16 electrode at 1 mA/cm^2. (c) EIS plots of NiBO-T10-16. (d) CV curves of NiBO-T13 at different scaning rates. (e) GCD curves of NiBO-T13 electrode at different current densities from 1 mA/cm^2 to 20 mA/cm^2. (f) Rate capabilities of NiBO-T13 at different scan rates. (g) Rate performance curve of NiBO-T13. (h) Cycle curve of NiBO-T13.

mation). SEM images of AM-NiBO-(10.12.14.16) are shown in Fig. S4 (Supporting information). No nanoarchitecture is observed for AM-NiBO-T10. With the time extends, there were exist some fine nanosheets for AM-NiBO-T12, and nanosheets of about 26 nm are observed for AM-NiBO-T13. For AM-NiBO-T14, the structure collapsedcollapses, and the structure began to aggregate into particles for AM-NiBO-T16. Electrochemical impedance spectroscopy (EIS) measurement in Fig. 4c is to study charge transfer rates and ion diffusion kinetics. The equivalent circuit is as shown in Fig. S5 (Supporting information), and AM-NiBO-T13 has equivalent series resistance (R_s) ($R_s = 0.045\ \Omega$) and lower resistive charge transfer (R_{ct}) ($R_{ct} = 0.019\ \Omega$) [25]. Other R_s and R_{ct} are shown in Table S1

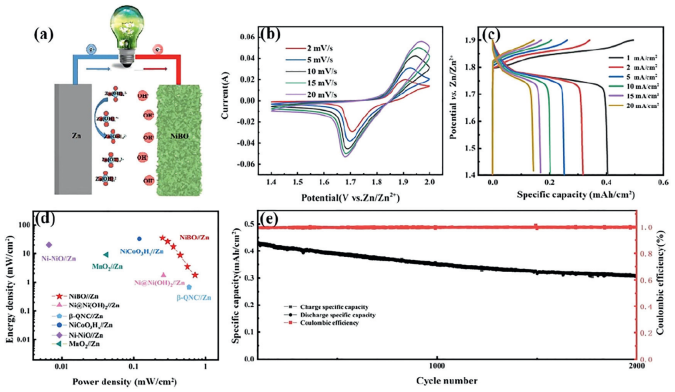

Fig. 5. (a) Schematic of AZIB based on AM-NiBO-T13 cathode and zinc anode. (b) CV curves and (c) GCD curves of zinc ion battery assembled with AM-NiBO-T13. (d) Graph of energy density and power density. (e) Cycle curves at 10 mA/cm^2.

(Supporting information). Through comparative experiments, it can be concluded that the time for 13h is appropriate for electrochemical corrosion in 0.1 mol/L $K_2B_4O_7$ solution.

In Fig. 4d, CV curves present almost the same shapes at different scanning rates. Two redox peaks at 0.28 V and 0.55 V are observed in CV curves, and the oxidation peak shifts to the higher potential and the reduction peak of the lower potential with the increase of scanning rates, which show good reversible Faraday reaction and rate performance. GCD curves in Fig. 4e for NiBO-T13 show that the charge/discharge curves exhibit a quasi linear voltage response as a function of Zn^{2+} concentration regardless of the magnification. The specific discharge capacities are calculated to be 0.65, 0.62, 0.55, 0.46, 0.36, 0.28 mAh/cm^2 at 1, 2, 5, 10, 15 and 20 mA/cm^2, respectively. Fig. 4f shows that the capacities of NiBO-T13 are as high as 0.65, 0.62, 0.55, 0.46, 0.36, 0.28 mAh/cm^2 at 1, 2, 5, 10, 15 and 20 mA/cm^2 corresponding well with the calculating values of GCD.

The rate performance of AM-NiBO-T13 electrode at different current densities (1–30 mA/cm^2) in Fig. 4g exhibit that its corresponding capacity retention rate is 86.9%, indicating good rate performance of AM-NiBO-T13. The cycle stability curves of AM-NiBO-T13 at 10 mA/cm^2 in Fig. 4h show that the capacity retention rate still remains 95.1% and a Coulomb efficiency is of 1 after 2000 cycles, indicating good cycle stability and high reversible capacity. It can be seen that its amorphous structure and boron oxygen bond in nickel borate are conducive to the cyclic stability of the material.

AM-NiBO-T13 is used as cathode to assemble rechargeable alkaline aqueous ZIBs, and the AM-NiBO-T13//Zn is assembled with AM-NiBO-T13 as cathode, zinc foil as anode, 3.0 mol/L KOH and 0.03 mol/L $Zn(CH_3COO)_2$ as electrolyte and non-woven cloth as separator, as shown in Fig. 5a. The corresponding electrochemical reactions in AM-NiBO-T13//Zn full battery is summarized as follows:

Cathode:

$$NiBO + xOH^- + H_2O \leftrightarrow NiB(OH)_{x+2} + xe^- \quad (1)$$

Anode:

$$Zn(OH)_4^{2-} + 2e^- \leftrightarrow Zn + 4OH^- \quad (2)$$

CV curves in Fig. 5b show that *quasi*-symmetric redox peaks keep good shapes and the areas gradually increase with the increase of scanning rates, revealing excellent reversibility. Fig. 5c shows the charge/discharge curves of AM-NiBO-T13 assembled zinc ion battery under various current densities, the capacities are 0.40, 0.31, 0.25, 0.20, 0.16 and 0.14 mAh/cm^2 at 1, 2, 5, 10, 15 and 20 mA/cm^2. The comparison of the two electrode capacities is shown in Fig. S6 (Supporting information). The excellent energy

storage capacity benefits from the following aspects: (1) Amorphous borate materials have nanosheet structure, high stability, fast charging speed and great energy storage potential; (2) The AM-NiBO exhibits large surface area and inherent abundant defects, which are beneficial for the diffusion of ions and fast collection and transport of electrons in the electrolyte; (3) Due to the existence of light boron in the nanosheets, the transition metal borates have high specific anisotropy. Boron can coordinate with oxygen atoms to form different groups with various structures. These characteristics can reduce voltage polarization and provide rich redox potential.

The Ragone plot in Fig. 5d and Table S2 (Supporting information) shows that its energy density can reach 0.77 mWh/cm^2 when the power density is 1.76 mW/cm^2 (0.25 mWh/cm^2 at 1.76 mW/cm^2), which are larger than some other reported AZIBs, such as the Ni@Ni(OH)$_2$//Zn (0.26 mWh/cm^2; 1.73 mW/cm^2) [51], β-QNC//Zn (0.59 mWh/cm^2; 0.67 mW/cm^2) [30], $NiCoO_3H_x$//Zn (0.12 mWh/cm^2; 32.7 mW/cm^2) [52], Ni-NiO//Zn (0.0066 mWh/cm^2; 20.2 mW/cm^2) [53] and MnO_2//Zn (0.042 mWh/cm^2; 9.1 mW/cm^2) [54]. In addition, the cycle performance in Fig. 5e shows that AM-NiBO-T13 based ZIB has good cycle performance after 2000 cycles and high capacitance retention (about 73% of the initial specific capacitance).

In summary, amorphous nickel borate nanosheets were synthesized on foam nickel by one-step constant voltage *in-situ* electrochemical corrosion method. AM-NiBO-T13 shows high capacity and cyclic stability as electrode with capacity of 0.65 mAh/cm^2 at 1 mA/cm^2 and with 95.1% capacity retention after 2000 cycles. The assembled AM-NiBO-T13//Zn shows a high capacity, large energy density and good stability (0.4 mAh/cm^2 at 1 mA/cm^2, 0.77 mWh/cm^2 at 1.76 mW/cm^2, 73% of the initial specific capacitance after 2000 cycles). The high stability, fast charging rate and great energy storage potential of AM-NiBO is due to its unique amorphous nanosheets structure and the coordination characteristics of boron and oxygen in borate materials. This study not only proves the potential application prospect of AM-NiBO nanosheets in zinc ion battery, but also paves the way for the rational design and manufacture of other transition metal borates with unique energy storage structure.

Declaration of competing interest

The authors declare that they have no known competing financial interests or personal relationships that could have appeared to influence the work reported in this paper.

Acknowledgments

This work was supported by the Independent Cultivation Program of Innovation Team of Ji'nan City (No. 2019GXRC011). All the authors discussed the results and commented on the manuscript.

References

[1] X. Zhang, G. Qu, Z. Wang, et al., Chin. Chem. Lett. 32 (2021) 2453–2458.
[2] C.X. Xu, J.J. Jiang, Rare Met. 40 (2021) 749–751.
[3] J. Shin, J.W. Choi, Adv. Energy Mater. 10 (2020) 2001386.
[4] X. Jia, C. Liu, Z.G. Neale, J. Yang, G. Cao, Chem. Rev. 120 (2020) 7795–7866.
[5] M. Song, H. Tan, D. Chao, H.J. Fan, Adv. Funct. Mater. 28 (2018) 1802564.
[6] B. Tang, L. Shan, S. Liang, J. Zhou, Energy Environ. Sci. 12 (2019) 3288–3304.
[7] J. Xie, Q. Zhang, Small 15 (2019) 1805061.
[8] J. Jiang, J. Liu, Interdiscip. Mater. 1 (2022) 116–139.
[9] C. Wang, S. Zhao, X. Song, et al., Adv. Energy Mater. 12 (2022) 2200157.
[10] X. Zeng, J. Hao, Z. Wang, J. Mao, Z. Guo, Energy Storage Mater. 20 (2019) 410–437.
[11] J. Ming, J. Guo, C. Xia, W. Wang, H.N. Alshareef, Mat. Sci. Eng. R. 135 (2019) 58–84.
[12] F. Xiong, Y. Jiang, L. Cheng, et al., Interdiscip. Mater. 1 (2022) 140–147.
[13] N. Zhang, X. Chen, M. Yu, et al., Chem. Soc. Rev. 49 (2020) 4203–4219.
[14] H. Pan, Y. Shao, P. Yan, et al., Nat. Energy 1 (2016) 16039.
[15] X. Zhu, Y. Wu, Y. Lu, et al., J. Colloid Interfaces Sci. 587 (2021) 693–702.
[16] Y. Yang, W.F. Wei, Rare Met. 39 (2020) 332–334.
[17] L. Zhu, B. Fei, Y. Xie, et al., ACS Appl. Mater. Interfaces 13 (2021) 22304–22313.
[18] J. Du, S. You, X. Li, et al., ACS Appl. Mater. Interfaces 12 (2020) 686–697.
[19] G.S. Kaliaraj, A. Ramadoss, Mat. Sci. Semicond. Proc. 105 (2020) 104709.
[20] H.R. Pouretedal, A. Norozi, M.H. Keshavarz, A. Semnani, J. Hazard. Mater. 162 (2009) 674–681.
[21] A. Rose, B. Shunmugapriya, T. Maiyalagan, T. Vijayakumar, J. Mater. Sci-Mater. El. 31 (2020) 19204–19212.
[22] M. Shahi, F. Hekmat, S. Shahrokhian, J. Colloid Interfaces Sci. 585 (2021) 750–763.
[23] H.K. Farag, M.A. Marzouk, J. Mater. Sci-Mater El. 28 (2017) 15480–15487.
[24] Y. Tao, Z. Li, L. Tang, et al., Electrochim. Acta 331 (2020) 135296.
[25] G. Xiang, Y. Meng, G. Qu, et al., Sci. Bull. 65 (2020) 443–451.
[26] X. Tong, Y. Li, N. Pang, et al., J. Energy Chem. 66 (2022) 237–249.
[27] D.A. Reddy, H. Lee, M. Gopannagari, et al., Int. J. Hydrog. Energy 45 (2020) 7741–7750.
[28] X. Wang, X. Zhang, G. Zhao, et al., ACS Nano 16 (2022) 6093–6102.
[29] J. Ye, L. Chen, Y. Shi, et al., ACS Appl. Energy Mater. 4 (2021) 12345–12352.
[30] T. Chen, Y. Bai, X. Xiao, H. Pang, Chem. Eng. J. 413 (2021) 127523.
[31] N. Li, G. Qu, X. Zhang, et al., Chin. Chem. Lett. 33 (2022) 3272–3276.
[32] T. Gupta, A. Kim, S. Phadke, et al., J. Power Sources 305 (2016) 22–29.
[33] Y. Jiang, M. Peng, J. Lan, et al., J. Mater. Chem. A 7 (2019) 21069–21078.
[34] P. Becker, Adv. Mater. 10 (1998) 979–992.
[35] J.L.C. Rowsell, L.F. Nazar, J. Mater. Chem. 11 (2001) 3228–3233.
[36] B. Xu, Y. Liu, J. Tian, et al., Chem. Eng. J. 363 (2019) 285–291.
[37] K. Zhou, G. Xu, Y. Chen, et al., Chem. Eng. J. 375 (2019) 121998.
[38] W. Qin, Y. Liu, X. Liu, G. Yang, J. Mater. Chem. A 6 (2018) 19689–19695.
[39] Y.J. Guo, P.F. Wang, Y.B. Niu, et al., Nat. Commun. 12 (2021) 5267.
[40] H.B. Li, M.H. Yu, F.X. Wang, et al., Nat. Commun. 4 (2013) 1894.
[41] Q. Li, Y. Xu, S. Zheng, et al., Small 14 (2018) 1800426.
[42] K.A. Owusu, L. Qu, J. Li, et al., Nat. Commun. 8 (2017) 14264.
[43] D.G. Tong, D. Wang, W. Chu, J.H. Sun, P. Wu, Electrochim. Acta 55 (2010) 2299–2305.
[44] Y. Xue, Q. Zhang, W. Wang, et al., Adv. Energy Mater. 7 (2017) 1602684.
[45] P. Sun, N. Li, C. Wang, et al., J. Power Sources 427 (2019) 56–61.
[46] T. Wang, S. Zhao, G. Qu, J. Leng, X. Xu, J. Colloid Interfaces Sci. 615 (2022) 293–301.
[47] C. Han, W. Cao, H. Si, et al., Electrochim. Acta 322 (2019) 134747.
[48] M. Liang, M. Zhao, H. Wang, Q. Zheng, X. Song, J. Mater. Chem. A 6 (2018) 21350–21359.
[49] J. Chen, J. Xu, S. Zhou, N. Zhao, C.P. Wong, Nano Energy 21 (2016) 145–153.
[50] J.J. Zhou, K. Li, W. Wang, et al., ACS Appl. Energy Mater. 3 (2020) 12046–12053.
[51] Z. Hao, L. Xu, Q. Liu, et al., Adv. Funct. Mater. 29 (2019) 1808470.
[52] Y. Huang, W.Shan Ip, Y. Lau, et al., ACS Nano 11 (2017) 8953–8961.
[53] Y. Zeng, Y. Meng, Z. Lai, et al., Adv. Mater. 29 (2017) 1702698.
[54] J. Liu, N. Nie, J. Wang, et al., Mater. Today Energy 16 (2020) 100372.